A Programmable Laboratory Testbed in Support of Evaluation of Functional Brain Activation and Connectivity

Randall L. Barbour, Harry L. Graber, *Member, IEEE*, Yong Xu, Yaling Pei, Christoph H. Schmitz, Douglas S. Pfeil, Anandita Tyagi, Randy Andronica, Daniel C. Lee, San-Lian S. Barbour, *Senior Member, IEEE*, J. David Nichols, and Mark E. Pflieger

***Abstract*—An important determinant of the value of quantitative neuroimaging studies is the reliability of the derived information, which is a function of the data collection conditions. Near infrared spectroscopy (NIRS) and electroencelphalography are independent sensing domains that are well suited to explore principal elements of the brain's response to neuroactivation, and whose integration supports development of compact, even wearable, systems suitable for use in open environments. In an effort to maximize the translatability and utility of such resources, we have established an experimental laboratory testbed that supports measures and analysis of simulated macroscopic bioelectric and hemodynamic responses of the brain. Principal elements of the testbed include 1) a programmable anthropomorphic head phantom containing a multisignal source array embedded within a matrix that approximates the background optical and bioelectric properties of the brain, 2) integrated translatable headgear that support multimodal studies, and 3) an integrated data analysis environment that supports anatomically based mapping of experiment-derived measures that are directly and not directly observable. Here, we present a description of system components and fabrication, an overview of the analysis environment, and findings from a representative study that document the ability to experimentally validate effective connectivity models based on NIRS tomography.**

Manuscript received May 04, 2011; revised October 28, 2011, December 03, 2011; accepted December 28, 2011. Date of publication February 03, 2012; date of current version March 16, 2012. This work was supported in part by DARPA project N66001-10-C-2008, in part by the New York State Department of Health, and in part by the National Institutes of Health/National Institute of Neurological Disorders and Stroke (NIH/NINDS) under Grant R42NS050007, Grant R44NS049734, and Grant R21NS067278.

R. L. Barbour, H. L. Graber, and Y. Xu are with the Department of Pathology, SUNY Downstate Medical Center, Brooklyn, NY 11203 USA and with NIRx Medical Technologies LLC., Glen Head, NY 11545 USA (e-mail: randall.barbour@downstate.edu; harry.graber@downstate.edu; yong.xu@downstate.edu)

D. S. Pfeil, A. Tyagi, and R. Andronica are with the Department of Pathology, SUNY Downstate Medical Center, Brooklyn, NY 11203 USA.

D. C. Lee is with the Department of Surgery, SUNY Downstate Medical Center, Brooklyn, NY 11203 USA and with the Empire Clinical Research Investigator Program, Department of Medicine, Interfaith Medical Center, Brooklyn, NY 11213 USA (e-mail: daniel.lee@downstate.edu).

Y. Pei and San-Lian S. Barbour are with NIRx Medical Technologies LLC, Glen Head, NY 11545 USA (e-mail: ypeinirx@gmail.com; sue.barbour@nirx.net).

C. H. Schmitz is with NIRx Medizintechnik GmbH, 13189 Berlin, Germany (e-mail: cschmitz@nirx.de).

M. E. Pflieger and J. D. Nichols are with Source Signal Imaging, Inc., San Diego, CA 92102 USA (e-mail: mep@sourcesignal.com; dnichols@sourcesignal.com).

Color versions of one or more of the figures in this paper are available online at http://ieeexplore.ieee.org.

Digital Object Identifier 10.1109/TNSRE.2012.2185514

***Index Terms*—Dynamic causal modeling, effective connectivity, encephalography (EEG), near infrared tomography, programmable head phantom.**

I. Introduction

TODAY, a growing stable of quantitative neuroimaging resources is being developed to support the exploration of a host of factors affecting behavior, the impact of disease, and strategies to overcome impairments. These systems vary widely in the type of energy sources and detection strategies deployed, sensitivity to intrinsic responses, form factor, and the range of environments that can be studied. Common are large-scale systems that support functional measures of hemodynamic responses [e.g., functional magnetic resonance imaging (fMRI)], weak magnetic signals associated with bioelectric behavior [magnetoencephalography (MEG)] or the distribution of radiolabeled ligands [single photon computed emission tomography (SPECT), positron emission tomography (PET)]. Different from these are two complementary sensing technologies that have the desirable attributes of inherently compact form factors and sensitivity to the principal phenomenologies of the brain that are associated with neuroactivation. Here we refer to near infrared spectroscopy (NIRS) and electroencephalography (EEG) for measures of the hemodynamic and bioelectric response, respectively.

Together, these attributes strongly support development of resources that can explore the mentioned elements affecting human activity while enabling studies in natural environments where the full range of behavior, in all its manifestations, can be systematically explored. While desirable, such environments and the goal of establishing resources suitable to operate in them will produce a host of new challenges.

A strategy commonly used for developing such resources is to implement appropriate sensing form factors and to test system performance under the relevant conditions. While straightforward, adoption of this approach to functional imaging studies can be problematic, because many of the interesting brain responses are not directly observable and instead rely on data inversion schemes whose stability and limitations are often not well appreciated. Adding to this is a general uncertainty regarding the expected response to a given cue. In contrast, structural imaging techniques are well validated, in part owing to

the ability to evaluate phantoms that span a range of resolution and contrast values and are longitudinally stable. Access to such resources is instrumental in guiding system development and for validating operator training and routine performance of deployed systems. Curiously, equivalent phantoms for functional imaging studies are generally not available. Undoubtedly, a complicating factor is the need to explore relevant features of interest which, in this case, span a wide range of dynamic responses.

We have previously developed a programmable dynamic phantom for hemodynamic studies [1]. The active element is an electrochromic cell (ECC) whose optical properties can be precisely adjusted electronically, and in doing so can mimic time-varying hemodynamic behaviors, either simple or complex, with excellent precision and speed. This capability is one part of a larger technology integration effort we have initiated that has as its principal aims the ability to: 1) generate and recover complex neurally derived macroscopic behaviors that, in general, are not directly observable; 2) implement these in a longitudinally stable, anthropomorphic head form that supports maximal translatability between laboratory-based and subject-based studies. The second objective is accomplished by employing the same sensing devices, headgear, and analysis resources as are used in human- or animal-subject studies to explore the programmable validating environment, which we refer to simply as the testbed.

We anticipate that access to the testbed will have benefits similar to those which stable phantoms have provided to the development of structural imaging methods: that it will serve as an excellent training environment for those new to the field, provide an objective basis for verifying routine system performance and aid in new system development.

In recognition of the complementary information provided by NIRS and EEG sensing technologies, here we have taken a second step in the development of a stable phantom. The constructed device has an anthropomorphic form similar to that of our original phantom [1], and it has the added feature of a conducting brain space that is composed principally of a naturally derived hydrogel and saline, is hermitically sealed, has been stabilized against biological degradation, and includes programmable source elements that serve as a network of electric dipoles (in addition to the aforementioned ECCs). Because our attention is directed at this time to exploring macroscopic behaviors, we have made no effort to consider the many complexities of the brain that exist on the microscopic and mesoscopic scales. Additionally, because phantoms for EEG studies have been previously described and are—at least for nonhermitically sealed forms—simple to construct [2], our attention here has been to explore the properties of the hemodynamic elements that have been chronically embedded in an otherwise corrosive environment (i.e., saline).

Yet another aim of the current report has been to document the associated resources that are needed to effect fully translatable studies. This has included development of integrated headgear and of an advanced data-analysis environment that employs a common brain space. Thus, the overall theme here is decidedly a technical report, with the added demonstration of recovery of complex, nonobservable hemodynamic responses. In this regard, attention is drawn to a previous report in the literature that also has sought to deploy a phantom for NIRS and EEG studies [3]. While potentially useful as a calibrating device, its simple open form factor (a plastic cylinder containing an aqueous medium, and static optical inclusions) does not support objective assessment of the translatability of integrated systems of the type considered here.

II. System Description and Performance

In the following, we describe the principal elements of the testbed and provide exemplary results that document their capabilities.

A. Programmable Head Phantom

1) Phantom Fabrication: Here, we have extended an earlier approach [1] by introducing into the phantom a "brain," which is composed of a hydrogel-based biopolymer with saline added to mimic impedances typical of real tissue [4], [5]. Compared to gelatin-based approaches [5], the selected material offers the advantage that it can be molded to yield mechanically robust forms that are easily handled without deformation, yet are composed of $>97\%$ water. Commonly available stabilizers are included in the molding process to inhibit bacterial and mold growth, and scattering and absorbing materials are added to provide physiologically plausible background optical properties. At the present time, with the possible exception of the use of the selected hydrogel, there is no reason to believe that the materials used for constructing the brain space confer any unique properties. That is, the TiO_2 and India Ink that we have used could easily be replaced with other widely used optical scattering and absorbing materials (e.g., Intralipid, other dyes [6]). Additionally, while hydrogels, of which there are many, may confer other possible advantages (see Section V), in many instances use of a saline-based gelatin brain form is likely equally suitable. In practice, we anticipate that more than one type of head phantom might be constructed, some having optical and bioelectrical properties intended to strongly mimic those of a real brain, while others could strongly deviate from these backgrounds as a basis for exploring limits on information recoverability.

A concurrent requirement for ultimate success of the testbed has been the development of fabrication techniques that provide for a hermetically sealed form. Briefly, fabrication of a completed structure is accomplished using a three-step process. First, a face-shell containing a brain cavity is formed from doped silicone (Fig. 1(A), left). Because uncured silicone is notoriously viscous, the introduction of additives (e.g., TiO_2, India Ink) requires careful attention to mixing and suitable degassing to ensure homogeneity. A wide range of silicone mixtures are commercially available that vary in their curing times, type of curing agent, resulting stiffness and opacity. Here, we have used QM Skin 30 (Quantum Silicones Specialties, Richmond, VA), although other types likely could yield similar final properties. The precise amount of added TiO_2 was not fixed, in recognition that the extent of microscopic adhesion of TiO_2 can vary. Nevertheless, our goal was to match the transmission properties of a 1% Intralipid solution in a 1 cm cuvette. A typical concentration was on the order of 250 mg/L. India Ink was added to a final concentration of 0.004% vol/vol. Comparisons of multidistance

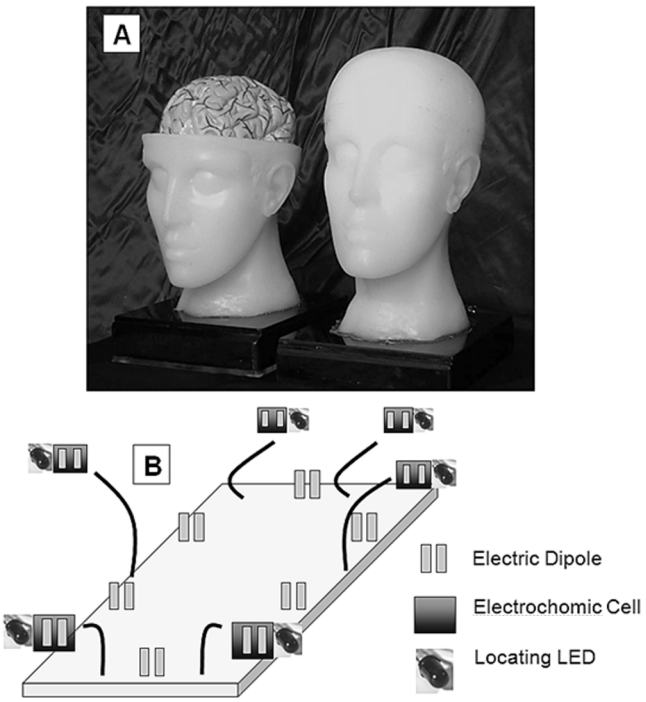

Fig. 1. (A) Partially formed and fully formed head phantom. (B) Schematic of embedded source array containing electric dipoles, ECCs and locating LEDs.

measures of optical intensity between the forehead of a human subject and the phantom revealed an attenuation profile similar to within an order of magnitude.

Next, the modeled brain, with included sources and attached wires [Fig. 1(B)], was introduced. A two-step process was used to fabricate the brain. First the source array was fabricated and tested for operation and electrical isolation. Next, the array was positioned within the brain mold, and liquefied hydrogel saline-based medium containing the mentioned optical additives and stabilizers was poured in. Prior to pouring, the mixture was vigorously stirred to ensure homogeneity. To avoid possible thermodegradation of the optical cells from prolonged exposure to the elevated temperatures needed to achieve liquefied hydrogel ($>80\,^{\circ}$C), the mold was first flash-heated by immersion into boiling water to prevent premature gel solidification upon subsequent introduction of the hydrogel, and then rapidly cooled by circulation of chilled water through a manifold embedded in all six sides of the mold.

Finally, upon introduction of a molded brain, containing a source array of the type sketched in Fig. 1(B), to the molded brain cavity (Fig. 1(A), left side) a silicone-based cranium was added to complete and seal the combined structure (Fig. 1(A), right side). To accomplish this without introduction of air, the brain-cavity, hydrogel brain assembly was positioned within the final cranial cavity-forming mold, and two-part mixed silicone was introduced slowly from the bottom, allowing the displacement of air through a small escape hole at the top of assembly. Allowing for curing times, fabrication of the entire assembly can be accomplished within a week, given a fully fabricated sensing array and support structures.

The human head-shaped phantom depicted in Fig. 1(A) was fashioned using a commercially available anatomical model of the head (American 3B Scientific, Tucker, GA, Model C25).

As currently configured, the source array includes a total of twelve electric dipoles, six ECCs and six LEDs that can be used to locate the sensor elements (which otherwise are unseen) in the completed phantom. The array employed here includes two different types of signal-generating arrangements. As depicted in the schematic [Fig. 1(B)]. one type features an ECC, dipole and locating LED within an integrated assembly having linear dimensions of $\sim$1.5 cm. The objective of this source configuration is to support modeling of induced neural signals and an accompanying local hemodynamic response. These assemblies are positioned in three roughly bilaterally symmetric locations, with elements positioned in the frontal, motor and occipital regions and oriented to follow the contour of the cranium at a depth of 1 cm into the cortex. This depth was adopted in recognition of the limits of NIR light penetration in the human head [7].

The other signal-generating arrangement includes only dipoles, which are positioned at greater depths (3–5 cm). This configuration was adopted in recognition that, in the real adult brain, deep-lying bioelectric sources are detectable by EEG, but not by NIRS measurements. Here we have introduced small-gauge wires leading from a central terminal positioned in the brain stem to connect to the dipoles and ECCs. Future forms will consider flexible printed circuit boards that can support high density arrays.

Control of the source array is achieved using a LabView GUI connected to a custom-made electronic driver that includes an expandable chassis with one or more 16-channel NI 9264 analogue output cards.

The dipoles were fashioned from pairs of gold-plated nickel pins, where each pin was 10 mm long and 0.5 mm in diameter, and the pair was separated by approximately 3 mm. In order to minimize electrical contact with the surrounding medium, the surface of the dipoles, except for the most distal 2 mm, were encased in nonconducting epoxy (as were any exposed electrical contacts associated with the optical cells and LEDs). Prior to encapsulation in the brain, the overall source array was tested for electrical isolation of components and for fidelity of operation.

Small-diameter rods composed of gold-plated nickel are used to access the conducting brain space from the surface, allowing use of simplified headgear arrangements (see subsequent description).

Testing of the optical elements has so far demonstrated no evidence of degradation of performance over a period of 12 months. In addition, excision of the entire source array from a selected phantom after a comparable time interval produced no evidence of component corrosion, mold or bacterial growth within the surrounding background matrix, or desiccation of the brain space.

Not shown are the driving electronics that can modulate each element of the array either individually or in combination, using either standard periodic waveforms (e.g., sine, square, triangle), or in accordance with user-designed time courses. The bioelectric sources can be driven at frequencies ranging from 0 (dc) to more than 1 kHz. The optical cells typically are driven over

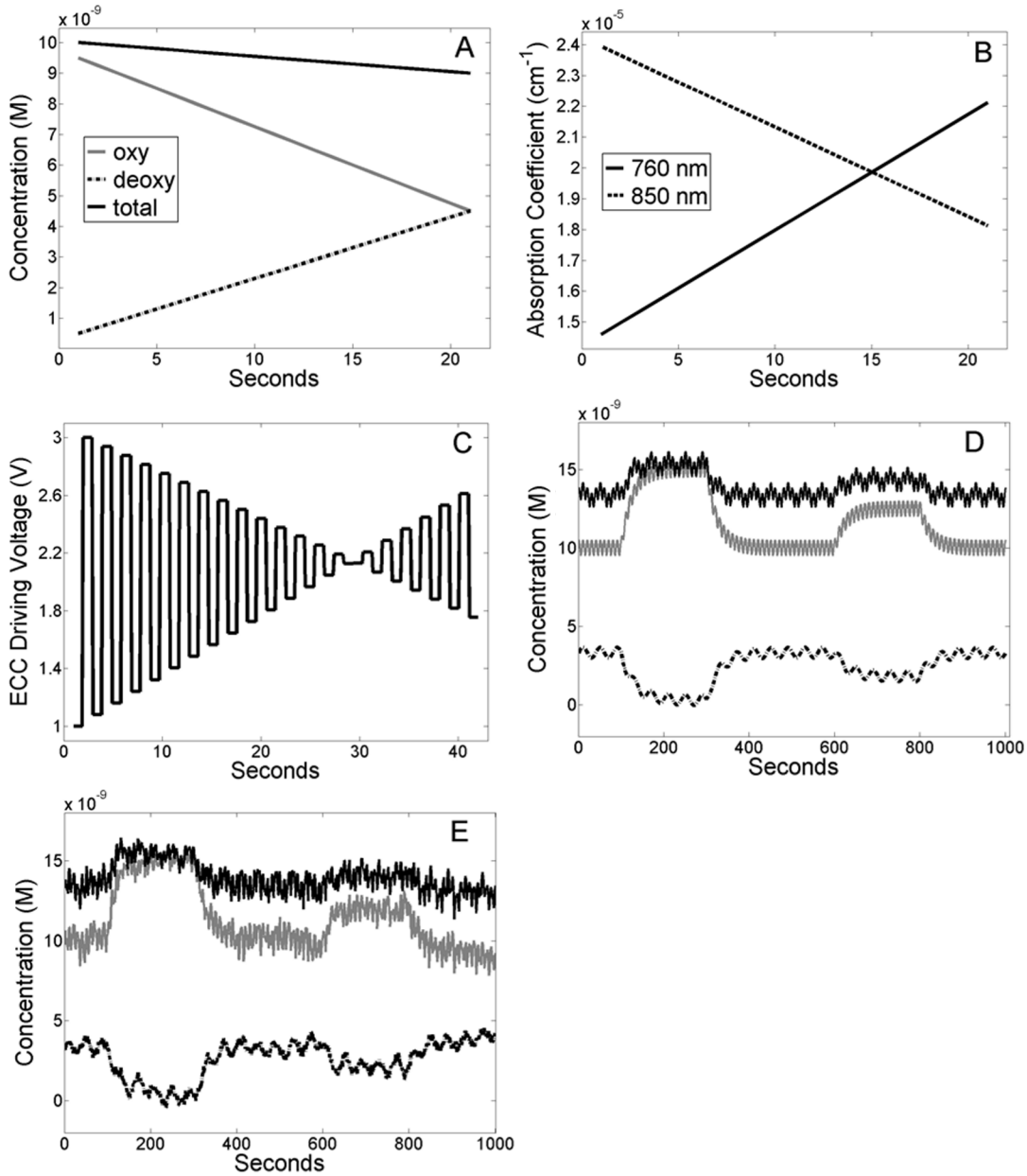

Fig. 2. Summary of the basic strategy for using the testbed dynamic phantom to simulate a hemodynamic response. Starting with the target hemodynamic time series (A), the corresponding two-wavelength absorption coefficients are computed (B), and then the appropriate voltage-versus-time sequence for driving the ECCs (C). (D) An idealized example of task-related hemodynamic responses, with physiological oscillations overlaid. (E) the recovered hemodynamic responses computed from testbed experimental data. Line-style coding in D and E is the same as that in A.

a frequency range of 0.01–2 Hz, which corresponds to physiologically important time scales, in order to model user-defined hemodynamic responses.

As currently configured, excepting the added sensors and attached wires, the brain space is otherwise homogeneous. Notably absent from the current phantom design is a skull. Because real bone is not feasible for commercial purposes, we are currently exploring use of porous plastics as a suitable substitute.

2) Generation of Endogenous Signals: Unlike the bioelectric signal, which is directly generated by application of a driving voltage to a dipole, generation of the hemodynamic signal is accomplished through a two-step process wherein the ECC driving voltage is toggled between two levels so that its opacity fluctuates between values corresponding to selected measuring wavelengths. Having a response time of <1 ms, the speed of switching can be adjusted to meet user-assigned hemodynamics or to simulate other optical phenomena (e.g., fast signal [8]).

An illustration and experimental demonstration of this modulation is shown in Fig. 2. Seen in Fig. 2(A) is an exemplary depiction of a hemoglobin (Hb) response, illustrating linear time dependence. Fig. 2(B) shows the corresponding variations in the optical coefficients, at two selected wavelengths, that are associated with this response. Plotted in Fig. 2(C) is the modulation of the ECC cell needed to achieve the Hb response shown in Fig. 2(A). Shown in Fig. 2(D) is a modeled signal modulation more typical of those seen in response to different conditions of neuroactivation. In particular, a BOLD-like response with superimposed added cardiac and respiratory rhythms is simulated. Shown in Fig. 2(E) is the recovered hemodynamic re-

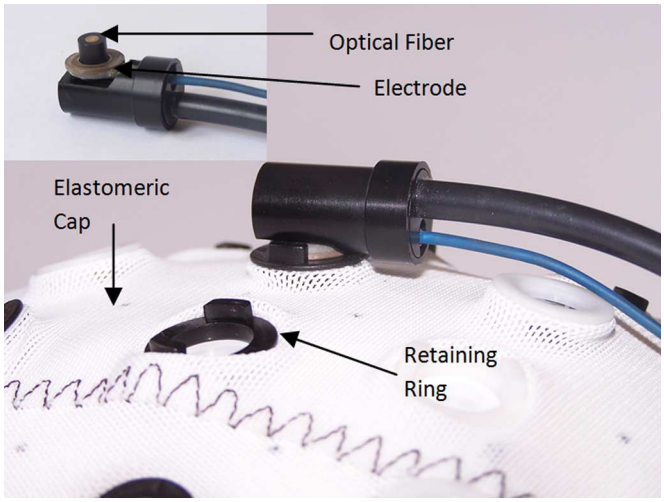

Fig. 3. Elastomeric cap with retaining rings used to hold the EEG electrode and NIR optode in place. Inset shows how the EEG electrode fits around the NIR optical fiber for co-located measurements.

sponse derived from the head phantom, where the detector data were generated using a timing sequence of the type illustrated in Fig. 2(C).

These results support previously reported findings that demonstrated that this solid-state approach can faithfully reproduce optical measures associated with true variations in Hb oxygenation, blood volume, or both, and the programmable phantom has excellent linearity, dynamic range, and operating life [1].

B. Hemodynamic-Bioelectric Headgear and Sensing

In line with establishing an integrated resource that maximally supports translation from the laboratory to subject studies, we have modified optode designs to allow for concurrent NIRS-EEG studies (e.g., see [9]) for several different commercially available headgear types. Shown in Fig. 3 is an example of one such type, while other optode-headgear designs are available [10]. Here, the optode design supports co-located EEG measures, which allows for higher sensor density configurations than can be achieved using adjacent sensor positioning. However, adjacent positioning offers the advantage of including additional hardware within the optode holder to more efficiently deal with hair displacement, reducing setup time. As a practical matter, we find that in human-subject studies, positioning a second elastomeric cap over the first with addition of a chin or chest straps serves to provide for highly stable sensor arrangements.

Typical sensor arrangements include standard 10–20 placements for both types of sensors, or use of high-density arrays. In the case of NIRS, the latter are necessary for tomographic studies. Both sensor types are increasingly available as scalable systems and have been adopted as wearable wireless systems [11]–[14]. In the case of EEG, these are available with either passive or active electrodes, while in the case of NIRS, the principal discriminating factors include various issues associated with different illumination-detection schemes. Similar to EEG, an aim for NIRS has been to achieve greater head coverage while retaining lightweight arrangements. This aim is best served by configurations that support active sensors in place of intervening optical fibers. Irrespective of these particulars, a key goal of the testbed design has been to enable substantial equivalency between phantom and subject-based measures (i.e., both use the same system hardware and headgear configurations).

C. NIRS-EEG Data Analysis and Mapping Environment

1) Near-Infrared Analysis Visualization and Imaging (NAVI): Modern data analysis pipelines applied to neuroimaging studies support a range of capabilities that include data editing and filtering, inversion schemes for localizing activities of interest (e.g., source localization, detection of hemodynamic response function), mapping capabilities based on either individualized information or on specified atlases, and the ability to define parametric maps for individual- or group-level statistical analyses. Such platforms also support a range of data-viewing options for raw and processed detector data, formed images, mosaics, etc. For the purpose of processing NIRS data, we have introduced NAVI [15], [16], which is a MATLAB-based environment that supports many of the principal data transformations common to evaluation of bioelectric and hemodynamic studies. A principal difference between NAVI and a roughly similar environment called NIRS-SPM [17] is that our approach is geared mainly toward supporting parametric atlas-based mapping with full 3-D tomographic capabilities, while NIRS-SPM presently is limited to only topographic measures of the sensor space.

The principal elements of NAVI include modules for image formation, display and analysis, an electronic ledger that automatically records metadata associated with the various data transformation resources, and important utilities. Among the latter are: GLM-based parametric mapping of detected hemodynamic response functions, modeled principally after strategies supported by SPM8 [18]; atlas-based mapping of image findings onto identified brain regions, with additional information provided by the automated anatomical labeling (AAL) functionality of SPM8 [19]; and examination of effective connectivity based on adoption of dynamic causal modeling (DCM) routines also available in SPM8.

Inversion resources employ fast and stable first-order 3-D reconstruction methods applied to the sensor time series [20]. Display capabilities support topographic displays of the sensor space, 3-D mapping registered to the anatomy, cortical maps involving interpolation of the latter, and montage views involving overlays of 10–20 positions and identification of specific brain regions by the AAL method.

2) ElectroMagnetic Source Estimation (EMSE): The EMSE Suite comprises software modules for integrating EEG (and MEG) with structural MRI [21]. The *Locator* module provides a convenient interface to 3-D digitizers for spatial mapping of sensor positions and MRI co-registration. The *Data Editor* module enables EEG review, with various spatial and temporal filters for treating artifacts. Data segments may be selected using experimental criteria to generate event-related summary measures in time, frequency, and time-frequency domains. These signal space measures are mapped topographically on the head surface via the *Visualizer* module, which also serves to display cortical current-density inverse-problem solutions (e.g.,

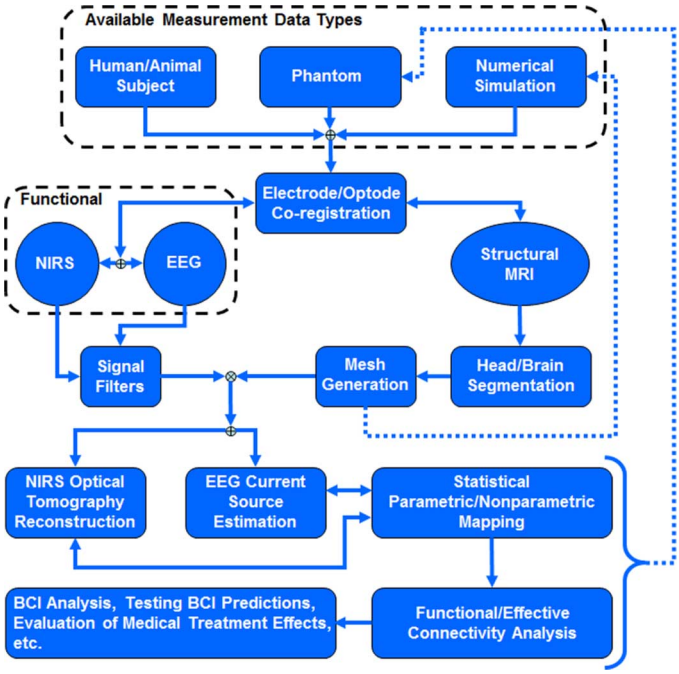

Fig. 4. Flowchart for integrated NIRS/EEG framework. The common anatomical framework is provided by structural MRI.

weighted minimum norm least squares [22], [23], sLORETA [24], [25], and linearly constrained minimum variance scanning beamformers [26]–[28]) provided by the *Source Estimator* module. *MR Viewer* provides MRI display capabilities, with tissue segmentation and mesh generation provided by *Image Processor*. Statistical nonparametric mapping (SnPM) via randomization of experimental conditions may be performed in either signal space or source space [29]–[31].

Shown in Fig. 4 is a flowchart of the currently available integrated analysis environment [32]. Key elements include: segmentation, registration and mesh generation resources applied to a common anatomical framework (provided by MRI); inverse solvers for both sensing domains; signal filtering; statistical parametric (individual- and group-level GLM) and nonparametric mapping (supported by separate domain or montage views); and, as is subsequently illustrated, additional processing in support of effective connectivity studies. Also indicated (dotted arrows) are the points where structural information and functional features derived from inverse-problem computations will feed back into available forward-problem solvers. This is intended to support computationally more intensive solutions for a given domain (e.g., coupled forward-inverse computations using nonlinear solvers), and coupled solutions *across* domains (e.g., DCM), for which primary data is available from the programmable phantom, while solution validation has thus far resisted systematic verification.

3) Atlas Based Mapping: Important goals of atlas-based studies are to provide an objective basis for identifying brain structures that undergo neuroactivation, and to support comparison of findings across data collection platforms, sensing modalities or other atlases. Solutions to either problem ideally would be based on knowledge of individualized boundary conditions. As in the case of EEG, in practice this requires access to anatomical information such as an individual's MRI data, as well as knowledge of sensor positions and head shape in relation to known fiducials. In addition to supporting objective mapping of sensor information, this information is also used to support forward computations of specified sensor arrays needed for inverse-problem computations. Explicit use of such capabilities requires access to an individual's MRI, which may or may not be available, and the processing resources needed to evaluate such information.

To support instances where MR images are not readily available, we have implemented an alternative solution wherein information from a selected atlas is substituted for individualized atlases. Using resources available in EMSE, we have generated a series of overlapping regions that support specification of any arbitrary sensor arrangement. Once the user has specified a given sensor arrangement, determination of the associated imaging operators is immediately available, thereby avoiding the multistep, labor-intensive effort needed to establish equivalent information from an individual atlas.

At this time, two atlases have been developed. One is based on a 26-year-old human male subject, and the other is derived from a group atlas obtained from 80 adult male and 32 adult female Rhesus macaques [33].

The developed atlases are depicted in Figs. 5 and 6. Having selected an atlas from an available menu, the GUI displays a specified head shape (human or macaque). Illustrated in Fig. 5(A) is the human atlas, which includes a montage of standard EEG electrode positions. Fig. 5(B) is a segmented cutaway illustration that contains a depiction of functional image data interpolated onto the cortical surface, along with a montage of the corresponding sensor array. Following manual or automated specification of the sensor array, the sensor locations are displayed on the selected atlas segment, as shown in Fig. 5(C). Precomputed elements associated with the specified optode array can then be retrieved from the library file in support of 3-D image reconstruction. Once computed, images are available for additional processing using features of SPM that have been modified to support NIRS data.

Shown in Fig. 6 is the approach adopted to generate the macaque atlas. As in the case of the human atlas, resources available from EMSE were employed to generate a segmented and tessellated array. A notable difference from the human-atlas case is the fact that we have substituted a group brain atlas for the individual brain [34], thereby generating a hybrid atlas, in order to minimize bias owing to anatomical peculiarities of the original subject. As with the human atlas, information corresponding to the associated imaging operators and reference detector readings needed for model-based image recovery are precomputed and accessible through a GUI.

An example of the spatial and temporal mapping capabilities achievable using the testbed is shown in Fig. 7. Here, tomographic data were collected from a macaque phantom [Fig. 7(D)], which included a natural-bone skull between the silicone "face" and "brain" compartments, with the latter containing a three-element internal ECC source array. A simple 1-Hz sine wave, applied to one selected ECC of the array, served as the driving function. In Fig. 7(A)–(C) we show mutually intersecting axial, coronal, and sagittal sections through

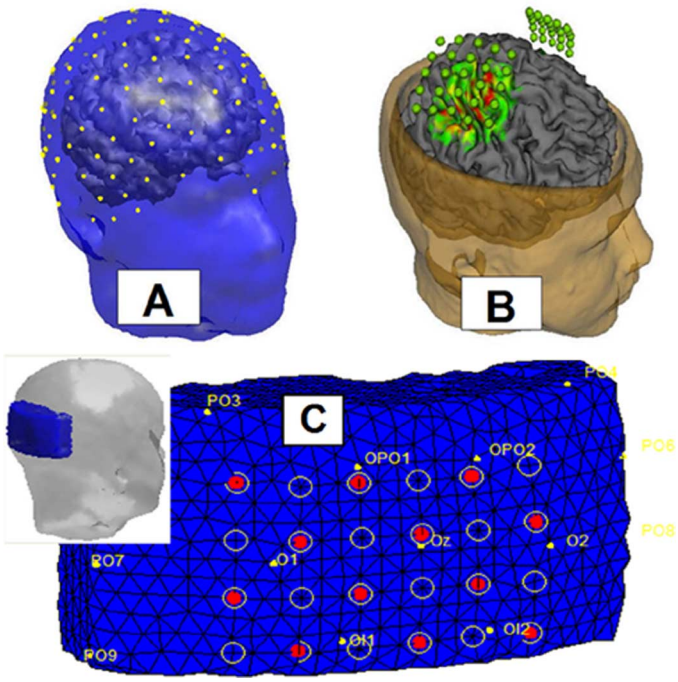

Fig. 5. Graphic summary of the developed human atlas. (A) Positions of the EEG electrodes. (B) 3-D representation of NIRS optode positions and a projection of hemodynamic information onto the cortex. (C) Example of an optode sensor array placement, displayed on a selected atlas segment. Open circles represent detector fibers only; filled circles are co-located source and detector. Yellow dots show standard EEG locations.

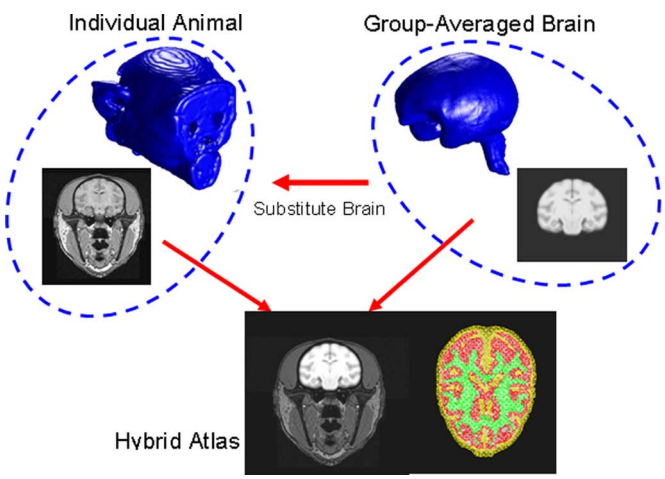

Fig. 6. Schematic showing the process used to create the macaque atlas. Information from a group-averaged brain is superimposed onto an individual MRI scan to yield the hybrid atlas. The image in the bottom right shows one of the segmented and tessellated slices from the atlas.

a reconstructed 3-D image, at one selected time point, of the simulated total Hb signal. Also shown [Fig. 7(E)] is the power spectral density of a single-pixel [indicated by the root of the arrow in Fig. 7(C)] time series extracted from the reconstructed image time series. The presented results thus demonstrate excellent fidelity of information recovery in both the spatial and temporal domains.

III. Exemplary Application

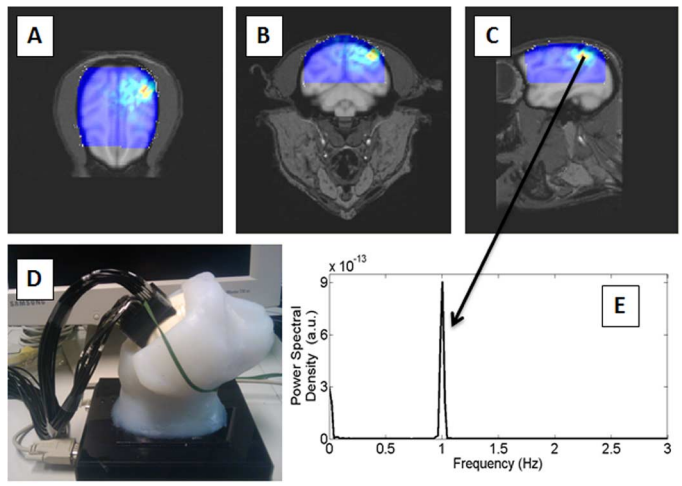

Fig. 7. Sample macaque phantom study. (D) shows a photograph of the phantom with fibers attached. (A) (B) and (C) show the horizontal, coronal, and sagittal views of the reconstructed image, highlighting the location of the ECC. (E) shows that after computing the PSD of the image time series, the 1 Hz sinusoidal driving function was recovered.

A. Testbed Simulation of Inter-Regional Connectivity

As indicated above, an important design feature of the phantom component of the testbed is that it provides users with exquisite control over the timing and amplitude of responses generated by the dipoles and ECCs. A practical consequence of the achieved degree of control is that it becomes possible to consider laboratory simulations involving higher-order brain functions that involve causally directed networks. In the real brain, such a network has the properties that: neural activity (and its hemodynamic correlates) of one region change in response to activity of others; that exogenous stimuli can affect a region's activity indirectly, through the influences it receives from the directly stimulated regions; and a given exogenous input needn't always have a direct effect on *any* of the regions involved in the network, but may instead influence their activities by temporarily altering, or modulating, the strengths of the excitatory and inhibitory connections among them [35].

As a demonstration of the claimed functional utility, here we select a model of coordinated hemodynamic activity that is based on an example previously reported in the fMRI literature [36]. The indicated study explored effective connectivity among three brain regions involved in processing visual information while four different exogenous-input conditions were applied in a pseudorandom sequence [37]. We chose this study as our point of departure because it allows us to demonstrate the multiple integrated resources needed to produce a laboratory simulation of such complex behavior. It also provides an explicit demonstration of the data quality and information content that can be recovered using the testbed. However, it is important to note that nothing in what follows is problem-specific. The same sequence of modeling, data collection, and data analysis would be followed for any application in which the goal is to use the testbed to evaluate the ability of an experiment-analysis protocol to accurately identify functional activity, such as interactions among brain regions.

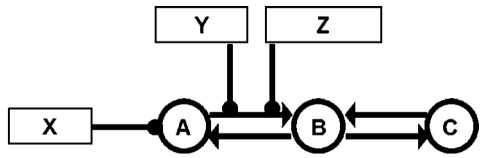

Fig. 8. Effective connectivity network modeled in DCM forward problem computations. The interregional connectivities and sites of action of the inputs are indicated. While the biological interpretations are arbitrary for the testbed demonstration, the neuroimaging study that serves as its historical launching point focused on three areas of the visual cortex ($\mathrm{A} = \mathrm{V1}$, $\mathrm{B} = \mathrm{V5}$, $\mathrm{C} = \mathrm{PPC}$) and three aspects of visual stimulus ($\mathrm{X} = \mathrm{present}$ versus absent, $\mathrm{Y} = \mathrm{moving}$ versus stationary, $\mathrm{C} =$ subject's attention directed versus not directed to the stimulus).

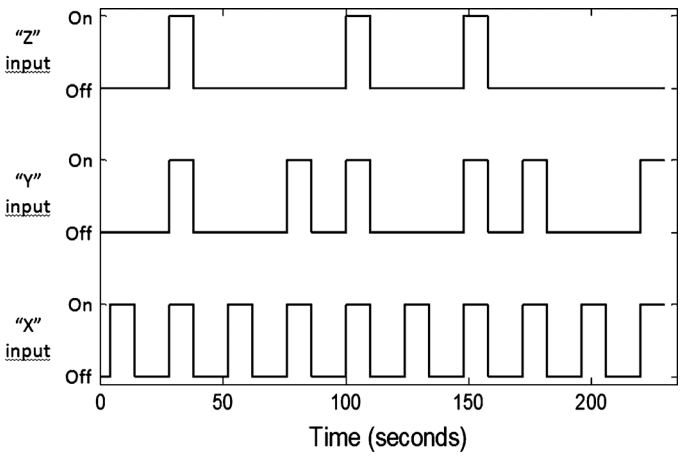

Fig. 9. Modeled time courses for the exogenous inputs depicted in Fig. 8.

For the testbed-based study, three ECCs of a dynamic phantom were driven with time-varying voltage signals, in order to simulate the blood-volume fluctuations occurring in three interacting cortical regions. The specific pattern of effective connectivity modeled is sketched in Fig. 8, which also shows the sites of action for the three exogenous inputs that induce neuroactivity-linked hemodynamic responses. It is seen that one of the inputs exerts a direct effect upon one of the regions, while the other inputs work by modulating the strength of an inter-regional interaction. The corresponding exogenous-input time courses are plotted in Fig. 9.

To compute the time-varying blood volume signals that were simulated by modulating the voltage across the phantom ECCs, we numerically solved the equations, presented in the following section, that are used to model neuroactivation and neurovascular coupling in DCM.

B. Analysis of Hemodynamic Responses With DCM

The problem of elucidating the interactions among multiple units in a network, based on observations of their composite behavior, arises in many contexts [38]. It has been found that many of the methods derived for analyzing network behavior in other fields can be successfully applied to the problem of inferring inter-regional interactions in the brain, *if* the data are obtained from direct measurements of the brain's electrical activity [35]. However, when the measurement assesses neural activity indirectly through its vascular correlates, then many of the techniques that are adequate for electrical data can give inaccurate results [39]. This is principally a consequence of the hemodynamic response function, which introduces a spatially heterogeneous time lag between any change in neural activity and its vascular correlates [39]. By contrast, DCM is a viable computational strategy even in this case, because it explicitly models the position-dependent time delay [35].

The basic approach in DCM is to update coefficients that model neural activity and associated neurovascular coupling in a manner that simultaneously considers the influence of external factors and the instantaneous bioelectric state. In practice this is accomplished using a Bayesian approach, wherein prior estimates of parameter values, and their variances and covariances, are iteratively updated for several candidate models to identify which best accounts for the observed behavior. The selection of a model is determined by comparing estimates of Bayesian model evidence derived from the posterior values of the parameters and of their variances and covariances [36].

For initial testing purposes, we used a straightforward bilinear mathematical model of the temporally evolving neuronal activity $\mathbf{x}$ in the regions that participate in an effective connectivity network [40]

$$\frac{d\mathbf{x}}{dt} = \left[\mathbf{A} + \sum_j u_j \mathbf{B}^{(j)}\right]\mathbf{x} + \mathbf{C}\mathbf{u}. \tag{1}$$

In (1), the dimensions of $\mathbf{x}$ and $\mathbf{u}$ are $N \times 1$ and $M \times 1$, respectively, where N is the number of interacting regions and M is the number of experimental inputs. The $N \times N$ matrix $\mathbf{A}$ specifies the inter-regional effective connectivity that is present even in the absence of external input; the $\mathbf{B}$ matrices (each $N \times N$) represent the modulating effects of experimental manipulations on the effective connectivity, and the $N \times M$ matrix $\mathbf{C}$ specifies the direct effects of the inputs on the regions' neural activities.

As our model of neurovascular coupling, we have used the following previously described model [40], which has frequently been employed in DCM analyses of fMRI data. The form of the model for any brain region is

$$\begin{aligned}
\frac{ds}{dt} &= x - \kappa s - \gamma(f-1) \\
\frac{df}{dt} &= s, \\
\frac{dv}{dt} &= \frac{1}{\tau}(f - v^{1/\alpha}) \\
\frac{dq}{dt} &= \frac{1}{\tau}\left[\frac{1-(1-E_0)^{1/f}}{E_0} f - \frac{q}{v} v^{1/\alpha}\right].
\end{aligned} \tag{2}$$

As neurovascular coupling involves interactions between neural activity and vasculature within a region but is not directly affected by the activities of the other regions, the neural activity variable changes from a vector $\mathbf{x}$ in (1) to a scalar x in (2). The remaining time-dependent variables in (2) are the vasodilatory signal associated with neural activity (s), inflow of blood (f), blood volume (v), and deoxyhemoglobin content (q). [Note that, as we are not evaluating fMRI data, no BOLD-signal equation is included in (2).] The variables f, v and q are normalized to their resting baseline levels (i.e., they are dimensionless and

are equal to 1 when $x = 0$). The parameters are the vasodilatory signal decay rate κ, autoregulatory feedback rate constant γ, mean capillary transit time τ, vessel stiffness exponent α, and the capillary resting net oxygen extraction E_0; the numerator term $1-(1-E_0)^{1/f}$ is a convenient approximation to the flow-dependent oxygen extraction.

When DCM is applied to NIRS measurement data, the goal is to solve an inverse problem: one or more hemodynamic variables (e.g., v or q) is supplied as input, and an iterative expectation-maximization (EM) algorithm is used to compute the parameter values (i.e., $\mathbf{A}, \mathbf{B}, \mathbf{C}, \kappa, \gamma, \tau, \alpha$, and E_0) that yield the most accurate fit to the data. The EM algorithm simultaneously evaluates the Bayesian evidence for the model, which is the basis for deciding which of several proposed effective connectivity networks is most strongly supported by the measurement data [36].

To explore the connectivity and associated hemodynamics of the considered problem using the testbed, we first specified the intrinsic ground-truth elements for the defined problem, against which alternative models of connectivity can be compared. Consequently, and also in order to guarantee convergence of (1) and (2), we used the coefficients derived from a DCM inverse calculation applied to the reported fMRI findings as the ground-truth interaction strengths [41], from which the corresponding time-dependent hemodynamic response was determined by solving the associated DCM forward problem. Armed with this information, the goal was to simulate this phenomenology using the dynamic phantom, then once again run DCM inverse computations, this time using several plausible connectivity models and the testbed-derived data for experimental input.

It should be noted that the various electronic elements of the phantom were *not* directly wired to each other in the manner depicted in Fig. 8 (or in any other way). That is, their ability to simulate the behavior of an effective connectivity network does not entail the manufacture of physical linkages among the phantom's active components. Instead, effective connectivity was modeled by supplying each ECC with an appropriate region-specific driving function, which had been precomputed by solving (1) and (2). The rapid response of the ECCs and the temporal precision that the controlling software provides makes this a workable strategy. Thus, any one phantom can be used to conduct experiments on a large number of distinct neuroimaging applications.

IV. Results

Human-Phantom Based Effective Connectivity Study

The time-varying voltage levels used to drive selected ECCs of the dynamic phantom are plotted in Fig. 10. These functions were obtained by solving the DCM forward problem described in the preceding section, then rescaling the computed normalized blood volume to lie within the cells' linear response ranges [1]. Shown in Fig. 11 is a mapping of image time series-derived dynamic feature information (GLM coefficients, as outlined subsequently) onto the cortical surface associated with the

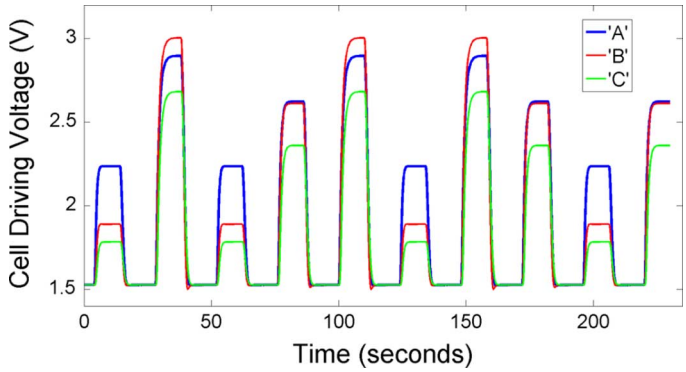

Fig. 10. Time courses of the driving voltages delivered to the ECCs that model the hemodynamic responses of the indicated cortical regions. Voltage values are proportional to tissue blood volume values computed by evaluating the DCM forward problem.

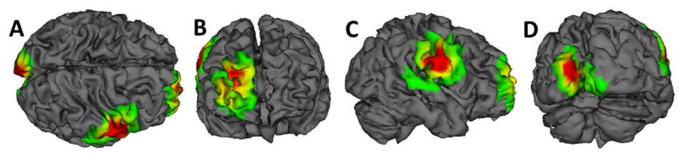

Fig. 11. Cortical surface mapping of GLM coefficients. Plotted quantity (arbitrary units) is the value of the GLM β coefficient obtained by fitting the appropriate ECC driving function to the tissue blood volume time series in each image pixel. A—top view, B—frontal view, C—right-side view, D—back view.

human-brain atlas. The red-colored regions indicate the locations of the three ECCs that were used for the laboratory simulation. It should be noted, however, that for the purposes of the demonstration the choice of which ECCs to use was arbitrary.

The two-wavelength data time series collected from the phantom were processed using NAVI-SPM. First, taking into account details of the optode arrays (such as the one depicted in Fig. 5, which was used for the data from optodes located over the occipital ECC), time series of 3-D images were reconstructed. Subsequently, statistical parametric maps, which are replotted in a different format in Fig. 11, were generated using the GLM methods available in Level-1 SPM; for each ECC, the corresponding function shown in Fig. 10 was used as the model function. Volume-averaged temporal responses (Fig. 12), obtained from the regions of interest identified by Level-1 SPM, were derived that served as the input for subsequent DCM inverse-problem computations. The three models depicted in Fig. 13 were used as alternative effective connectivity hypotheses. For each hypothesis, DCM iteratively updates the coefficients in (1) and (2) in order to achieve the best fit it can between the experimental and computed values of the variable v. In addition, it computes a model selection-criterion value, which is a function of the achieved accuracy as well as of the complexity of the model [35]. When the three networks in Fig. 13 are compared, the correct model is the one preferred on the basis of the model selection criterion.

In a similar spirit, the effects of physiological "noise" (i.e., fluctuations in the hemodynamic variables that are not associated with the phenomenology of interest) can be experimentally evaluated. A straightforward approach for doing so is illustrated in Fig. 14, where a set of ECC driving functions is plotted that

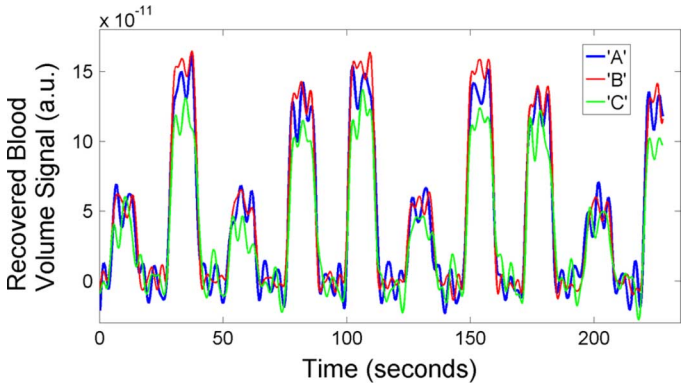

Fig. 12. Spatial mean time series of recovered tissue blood volumes, for each of the three brain regions considered. Averages are computed over all image pixels that have a statistically significant ($p < 10^{-6}$) GLM fit to the corresponding driving function shown in Fig. 10.

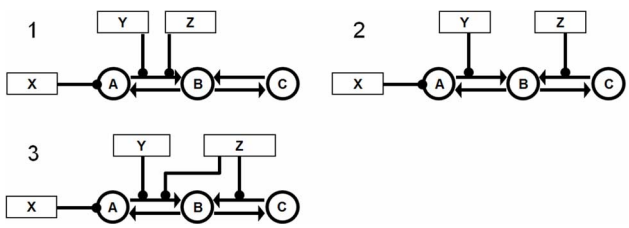

Fig. 13. The three effective connectivity networks that are supplied as inputs to the DCM inverse problem code, as plausible hypotheses for the connectivity present in the testbed model. For the phantom experiment, it is known a priori that the network in (A), reproduced from Fig. 8, is correct. For the DCM inverse-problem results obtained from the data in Fig. 12, the correct model's (1) log-evidence value is larger than those for the two alternative hypotheses by either 103 (2) or 89.4 (3) units.

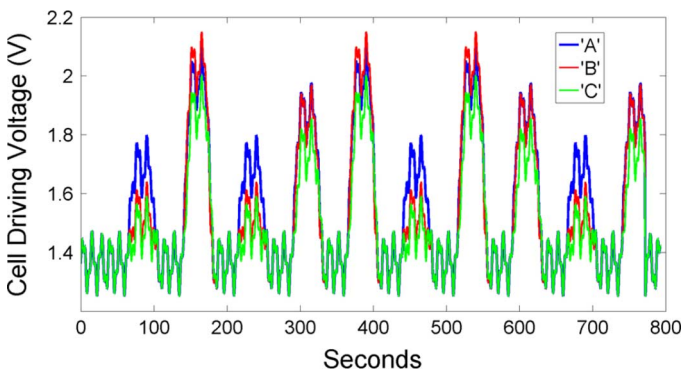

Fig. 14. ECC driving functions for second experiment. Background respiratory and vasomotor rhythms are added to the ideal-model behavior shown in Fig. 10. Color coding is the same as in Fig. 10.

model background respiratory and vasomotor rhythms in addition to the variations associated with task-related neuroactivation (cf. Fig. 10).

The effective connectivity simulation experiment was carried out a second time, with the ECC driving functions in Fig. 14 substituted for those in Fig. 10. If the resulting measurements are treated in the same manner as described for the "noise-free" data set, *without* processing the data to remove the contributions of the background rhythms [Fig. 15(A)], the consequence is complete loss of accuracy of the model selection procedure: effective connectivity network #3 in Fig. 13 is the one preferred

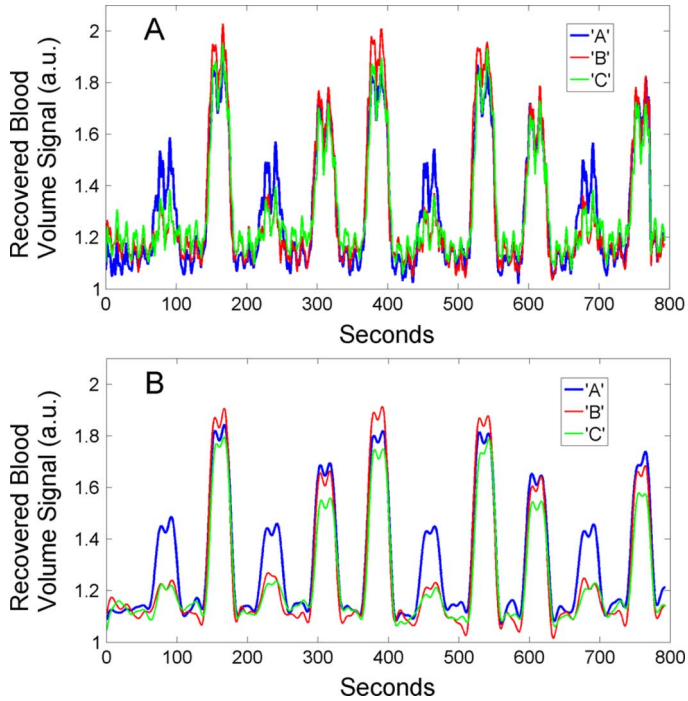

Fig. 15. (A) Reconstructed image-derived time series used as input for the DCM inverse computations for the second experiment. Color coding is the same as in Fig. 12(A). In addition to the protocol-related component, substantial contributions from background respiratory and vasomotor rhythms are evident. (B) Result obtained when time series in 15 A are low-pass filtered to reduce the amplitudes of background rhythms.

based on the model selection criterion, while the correct network (Fig. 13, #1) is the one judged least likely to be correct (log-evidence value for model 1 is smaller than those for models 2 and 3 by 19.8 and 25.4 units, respectively). However, if the image-derived hemodynamic time series are low-pass filtered prior to the DCM inverse-problem computations (more sophisticated algorithms for separating the components of a mixed signal that are and are not protocol-related are available, for cases where a simple frequency filter is not adequate [42], [43]), as indicated in Fig. 15(B), then the ordering shown in Fig. 13 is restored, and the correct network is the one selected (log-evidence value for model 1 is larger than those for models 2 and 3 by 39.5 and 5.2 units, respectively).

An important feature of above studies, in comparison to results obtained by computer simulation, is that because the former uses the same headgear, sensor arrangements, and measuring systems as deployed in any human or corresponding animal study, all of the experimental biases associated with real experiments are preserved. This carryover is critical when it comes to appreciating limits on information extraction, especially those involving information that is not directly observable (e.g., effective connectivity).

V. Discussion

Functional imaging methods are increasingly being applied to define localized and coordinated responses involving sensory, motor, and higher-order executive functions of the brain, in efforts to not only recognize associated responses but to serve as

metrics that can be used to develop a host of practical applications [44].

Sensing technology available to explore intrinsic signals, comprising bioelectric and hemodynamic responses, fall into two broad categories: systems comprising large-scale, costly and fixed facilities (e.g., MRI, MEG) and systems that deploy economical and increasing portable technology (e.g., fNIRS and EEG). From an information gathering perspective, a major attraction of the latter is the ability to perform studies in open environments wherein the full spectrum of task-dependent sensory and motor input and corresponding cognitive elements can be harnessed.

Here, we have described elements of a new experimental testbed that is intended to support evaluation of the principal observable elements of neural activity using hemodynamic and bioelectric sensing methods. The developed fabrication techniques are easily adopted to support generation of anatomically accurate forms that are longitudinally stable and contain embedded sources that are freely programmable. When operated together with the developed analysis environment, the configured system is intended to meet various practical needs as well as modeling of complex macroscopic neural phenomenologies.

A. Potential Practical Uses of the Testbed

The testbed described here has been developed to serve several useful purposes. At the most basic level it should serve as a teaching environment for those new to the field. The same sensing hardware, headgear and analysis environment used to explore the head phantom is used in subject-based studies. This homogeneity also maximizes translatability from laboratory to real-world applications. As currently constructed, the head phantom operates as a deterministic device. However, unlike numerical simulations where output is a deterministic function of input, here the output is expressly influenced by all of the real-world limitations that will attend subsequent use of the measuring system. For instance, in addition to data fidelity being affected by the performance characteristics of the sensing hardware and embedded sources arrays, it is also a function of particulars of the sensor-populated headgear. Variations in placement, contact, effects of ambient noise sources and other factors can all be expected to affect data quality. We believe such considerations have added significance when the goal is to explore nonobservable phenomenologies such as the effective connectivity example presented here. Inverting this consideration, if features of interest cannot be successfully recovered using the testbed, it is hard to imagine that improved success will be achieved in subject studies. At a minimum, exploration of the testbed should serve as a useful guide as to what types of studies are feasible.

Another potential use of the testbed is its ability to objectively determine the practical limits to information recovery. Measures of functional brain connectivity explored by noninvasive techniques, for example, are "twice-removed" from direct observation; first, the origins of activation are identified by inverting surface-derived sensor data; second, connectivity is identified by solving a dynamical system identification problem based on results obtained from the first inversion. In NIRS and EEG neuroimaging applications, both inverse problems are plagued by ill-posedness. In addition, the first, representing a boundary-value problem, can be strongly affected by incomplete knowledge regarding the details of the boundaries (internal and external). Here, the ability to expressly employ digitizing methods and to operate on individualized MR data sets certainly should aid in reducing errors originating from boundary condition mismatches. These additional capacities, combined with the fidelity with which endogenous signals can be generated, provide a solid basis for ground-truth benchmarking and for refinement of various feature extraction efforts.

Because of its longitudinal stability, still another practical use of the testbed is its ability to function as a routine quality assurance indicator for measuring systems. Quality assurance measures are, among other things, a significant factor in determining whether new technology can receive FDA approval. Here, our documentation of longitudinal stability admittedly has been limited when compared to validation standards typical for approved medical devices. We observed no obvious degradation in performance of the phantom over a one-year period, and a forensic inspection of extracted source arrays over a similar period failed to reveal any obvious biological degradation, component corrosion or desiccation of the brain space. This is expected, due to the selected materials and fabrication methods.

Yet another potential practical use of the testbed is its potential to serve as an information transfer hub for exploring brain–machine interface applications. Real sensor recordings, noninvasive or otherwise, can be introduced into the embedded source array and measured from the surface. The resulting real-time recordings can be operated on by selected processing schemes that then drive peripheral devices, thereby validating the fidelity and reproducibility of information transfer.

The suggested use to assist in real-time interpretation applications can be abstracted to various time-critical clinical decisions. A concrete example is the ambiguities confronting clinicians managing cases of acute stroke, where it is important to distinguish between ischemic and hemorrhagic stroke. Current standard-of-care procedures call for adoption of structural imaging methods to rule out the latter. While CT imaging is effective for appreciating hemorrhagic stroke, the added sensitivity of MR imaging supports improved delineation of the penumbra of ischemic stroke. Unfortunately, there are many situations where MR measures are infeasible on stroke victims, due to implanted metal [46]. Both NIRS and EEG have been demonstrated to be sensitive to the presence of stroke [47], [48], which has been shown to produce measurable changes in effective connectivity [49]. Building on its use as a quality assurance indicator and as objective tool for appreciating limits on information recovery, it seems entirely feasible that the testbed could serve as a real-time aid to assess, at a minimum, whether collected data is of sufficient quality to support an actionable clinical decision.

Continuing with this consideration, while the selected connectivity demonstration considered a mainly arbitrary ECC configuration, data were obtained, nevertheless, under conditions that at least grossly approximate those expected for a real head. Additionally, because the selected regions—prefrontal, motor and occipital cortex—are involved in the planning and execution of visually directed motor tasks, all elements that are affected in, for example, Parkinson's disease [50], these find-

ings at least suggest the feasibility of exploring disturbances in causally directed activity associated with this disease [51].

B. Limitations of the Testbed

Representing principally a deterministic tool having a limited number of fixed-placed embedded sources, it is instructive to compare the expected range of phenomenology that can be considered relative to that potentially available using a sophisticated simulation resource. Key discriminators here are the physical accuracy with which observed phenomenologies can be produced, the flexibility for reconfiguring internal sources, and the capacity to accurately account for real-world effectors. Favoring a simulation environment is the expected added flexibility to reconfigure source conditions. Which domain is favored for physical accuracy depends on several factors.

On a gross level, however, the testbed should hold the advantage because data obtained from it is experimentally derived using resources that are maximally translatable, at least for the sensor space. Internally, the demonstrated ability of the ECCs to produce complex hemodynamic responses with high fidelity, and likewise the expected fidelity of electric dipoles, would also suggest that a wide range of phenomenology can be faithfully introduced.

Admittedly, it seems unlikely that the testbed as currently configured would compare well to the suggested simulation environment for mesoscopic and microscopic phenomenology. That said, it has not escaped our attention that hydrogel-based media have proven an effective approach to sustaining populations of neurons, including in the presence of nanofabricated programmable circuitry [52]. When configured within an appropriately designed perfusion chamber, measures of real neural activity seems possible.

Thus far, our developmental focus has been to build out the primary elements of the testbed, including portable-wearable NIRS systems [11], headgear for concurrent NIRS-EEG studies [53], an integrated atlas-based analysis environment [34], and the phantom itself. In terms of the latter, it is relatively straightforward to fine-tune the background optical and impedance properties to achieve improved matching to real subjects. Previously mentioned is the need to introduce a skull. Higher-order considerations include the introduction of high-density source arrays for both hemodynamic and bioelectric domains, and improved precision of fabrication to ensure precise knowledge of their locations. Given such improvements, the testbed could be used to systematically explore the limits on source localization and other metrics as a function of the sensor space and applied computational effort.

REFERENCES

[1] R. L. Barbour, R. Ansari, R. Al Abdi, H. L. Graber, M. B. Levin, Y. Pei, C. H. Schmitz, and Y. Xu, R. J. Nordstrom, Ed., "Validation of near infrared spectroscopic (NIRS) imaging using programmable phantoms," in *Design and Performance Validation of Phantoms Used in Conjunction With Optical Measurements of Tissue (Proceedings of SPIE, Vol. 6870)*, 2008, Paper 687002.

[2] D. L. Hamblin, V. Anderson, R. L. McIntosh, R. J. McKenzie, A. W. Wood, S. Iskra, and R. J. Croft, "EEG electrode caps can reduce SAR induced in the head by GSM900 mobile phones," *IEEE Trans. Biomed. Eng.*, vol. 54, pp. 914–920, 2007.

[3] R. J. Cooper, R. Eames, J. Brunker, L. C. Enfield, A. P. Gibson, and J. C. Hebden, "A tissue equivalent phantom for simultaneous near-infrared optical tomography and EEG," *Biomedical Optics Express*, vol. 1, pp. 425–430, 2010.

[4] T. C. Ferree, P. Luu, G. S. Russell, and D. M. Tucker, "Scalp electrode impedance, infection risk, and EEG data quality," *Clin. Neurophys.*, vol. 112, pp. 536–544, 2001.

[5] R. M. Leahy, J. C. Mosher, M. E. Spencer, M. X. Huang, and J. D. Lewine, "A study of dipole localization accuracy for MEG and EEG using a human skull phantom," *Electroencephalogr. Clin. Neurophysiol.*, vol. 107, pp. 159–173, 1998.

[6] M. Firbank and D. T. Delpy, "A design for a stable and reproducible phantom for use in near-infrared imaging and scpectroscopy," *Phys. Med. Biol.*, vol. 38, pp. 847–853, 1993.

[7] A. H. Hielscher, R. E. Alcouffe, and R. L. Barbour, "Comparison of finite-difference transport and diffusion calculations for photon migration in homogeneous and heterogeneous tissues," *Phys. Med. Biol.*, vol. 43, pp. 1285–1302, 1998.

[8] A. V. Medvedev, J. Kainerstorfer, S. V. Borisov, R. L. Barbour, and J. VanMeter, "Event-related fast optical signal in a rapid object recognition task: Improving detection by the independent component analysis," *Brain Research*, vol. 1236, pp. 145–158, 2008.

[9] S. Fazli, J. Mehnert, G. Curio, A. Villringer, K.-R. Müller, J. Steinbrink, and B. Blankertz, "Enhanced performance by a hybrid NIRS-EEG brain computer interface," *Neuro Image*, vol. 59, pp. 519–529, 2012.

[10] [Online]. Available: http://www.brainproducts.com/productdetails.php?id=28&tab=1

[11] C. H. Schmitz and S. P. Koch, "Ultracompact, EEG-compatible NIRS system," in *Poster C 05 at the Berlin Brain Computer Interface Workshop*, Berlin, Germany, July 8–10, 2009 [Online]. Available: http://otg.downstate.edu/Publication/SchmitzBBCIW09.pdf

[12] G. Yurtsever, A. Bozkurt, F. Kepics, K. Pourrezaei, and A. Devaraj, "Pocket PC based wireless continuous wave near infrared spectroscopy system for functional imaging of human brain," in *Proc. 25th Annual International Conference of the IEEE Engineering in Medicine and Biology Society*, 2003, vol. 4, pp. 3435–3437.

[13] R. Lin, R.-G. Lee, C.-L. Tseng, Y.-F. Wu, and J.-A. Jiang, "Design and implementation of wireless multi-channel EEG recording system and study of EEG clustering method," *Biomedical Engineering—Applications, Basis & Communication*, vol. 18, pp. 276–283, 2006.

[14] "Eight-channel wireless EEG system for ambulatory monitoring developed," ScienceDaily Oct. 6, 2009, Interuniversity Microelectronics Centre (IMEC), Web. 20 Oct. 2011.

[15] Y. Pei, Z. Wang, and R. L. Barbour, "NAVI: A problem solving environment (PSE) for NIRS data analysis," Poster No. 685 T-AM at Human Brain Mapping 2006. Florence, Italy, June 11–15, 2006 [Online]. Available: http://otg.downstate.edu/Publication/PeiHBM06.pdf

[16] *NIRx fNIRS Analysis Environment User's Guide*, [Online]. Available: http://otg.downstate.edu/Publication/NIRxPackage_02.pdf

[17] J. C. Ye, S. Tak, K. E. Jang, J. Jung, and J. Jang, "NIRS-SPM: Statistical parametric mapping for near-infrared spectroscopy," *NeuroImage*, vol. 44, pp. 428–447, 2009.

[18] W. D. Penny, K. J. Friston, J. T. Ashburner, S. J. Kiebel, and T. E. Nichols, *Statistical Parametric Mapping: The Analysis of Functional Brain Images*. : Academic Press, 2006.

[19] N. Tzourio-Mazoyer, B. Landeau, D. Papathanassiou, F. Crivello, O. Etard, N. Delcroix, B. Mazoyer, and M. Joliot, "Automated anatomical labeling of activations in SPM using a macroscopic anatomical parcellation of the MNI MRI single-subject brain," *NeuroImage*, vol. 15, pp. 273–289, 2002.

[20] Y. Pei, H. L. Graber, and R. L. Barbour, "Influence of systematic errors in reference states on image quality and on stability of derived information for DC optical imaging," *Applied Optics*, vol. 40, pp. 5755–5769, 2001.

[21] Source Signal Imaging, Inc., EMSE Suite User Manual, Version 5.4. San Diego, 2011 [Online]. Available: ftp://ftp.sourcesignal.com/manuals/

[22] I. F. Gorodnitsky, J. S. George, and B. D. Rao, "Neuromagnetic source imaging with FOCUSS: A recursive weighted minimum norm algorithm," *Electroencephalogr. Clin. Neurophysiol.*, vol. 95, pp. 231–251, 1995.

[23] H. Liu, X. Gao, P. H. Schimpf, F. Yang, and S. Gao, "A recursive algorithm for the three-dimensional imaging of brain electric activity: Shrinking LORETA-FOCUSS," *IEEE Trans. Med. Imag.*, vol. 10, pp. 1794–1802, 2004.

[24] R. D. Pascual-Marqui, "Standardized low resolution brain electromagnetic tomography (sLORETA): Technical details," *Meth. & Findings in Exp. & Clin. Pharm.*, vol. 24D, pp. 5–12, 2002.
[25] M. Wagner, M. Fuchs, and J. Kastner, "Evaluation of sLORETA in the presence of noise and multiple sources," *Brain Topography*, vol. 16, pp. 277–280, 2004.
[26] B. D. Van Veen, W. van Drongelen, M. Yuchtman, and A. Suzuki, "Localization of brain electrical activity via linearly constrained minimum variance spatial filtering," *IEEE Trans. Biomed. Eng.*, vol. 44, pp. 867–880, 1997.
[27] V. Murzin, A. Fuchs, and J. A. S. Kelso, "Anatomically constrained minimum variance beamforming applied to EEG," *Exp. Brain. Res.*, vol. 214, pp. 515–528, 2011.
[28] R. E. Greenblatt, A. Ossadtchi, and M. E. Pflieger, "Local linear estimators for the bioelectromagnetic inverse problem," *IEEE Trans. Sig. Proc.*, vol. 53, pp. 3403–3412, 2005.
[29] R. C. Blair and W. Karniski, , R. W. Thatcher, Ed. *et al.*, "Distribution-free statistical analyses of surface and volumetric maps," in *Functional Neuroimaging: Technical Foundations*. San Diego: Academic Press, 1994, pp. 19–28.
[30] E. Maris and R. Oostenveld, "Nonparametric statistical testing of EEG- and MEG-data," *J. Neurosci. Meth.*, vol. 164, pp. 177–190, 2007.
[31] R. E. Greenblatt and M. E. Pflieger, "Randomization-based hypothesis testing from event-related data," *Brain Topography*, vol. 16, pp. 225–232, 2004.
[32] R. L. Barbour, J. Mehnert, Y. Xu, H. L. Graber, J. D. Nichols, A. Ossadtchi, and M. E. Pflieger, "Software for integrated analysis of NIRS-EEG data," in *Paper NIH100-53 at the 7th NIH Inter-Institute Workshop on Optical Diagnostic and Biophotonic Methods from Bench to Bedside*, Bethesda, MD, Sept. 15–16, 2011 [Online]. Available: http://otg.downstate.edu/Publication/BarbourNIH11.pdf
[33] D. G. McLaren, K. J. Kosmatka, T. R. Oakes, C. D. Kroenke, S. G. Kohama, J. A. Matochik, D. K. Ingram, and S. C. Johnson, "A population-average MRI-based atlas collection of the rhesus macaque," *NeuroImage*, vol. 45, pp. 52–59, 2009.
[34] Y. Xu, D. S. Pfeil, T. Gevorgyan, D. C. Lee, and R. L. Barbour, "3-D DOT brain imaging for rhesus monkey: An anatomical atlas-based method," in *Paper NIH100-55 at the 7th NIH Inter-Institute Workshop on Optical Diagnostic and Biophotonic Methods from Bench to Bedside*, Bethesda, MD, Sept. 15–16, 2011 [Online]. Available: http://otg.downstate.edu/Publication/XuNIH11.pdf
[35] K. Friston, "Causal modeling and brain connectivity in functional magnetic resonance imaging," *PLoS Biology*, vol. 7, pp. 0220–0225, 2009.
[36] W. D. Penny, K. E. Stephan, A. Mechelli, and K. J. Friston, "Comparing dynamic causal models," *NeuroImage*, vol. 22, pp. 1157–1172, 2004.
[37] C. Büchel and K. J. Friston, "Modulation of connectivity in visual pathways by attention: Cortical interactions evaluated with structural equation modelling and fMRI," *Cereb. Cortex*, vol. 7, pp. 768–778, 1997.
[38] T. G. Lewis, *Network Science: Theory and Applications*. : Wiley, 2009.
[39] O. David, I. Guillemain, S. Saillet, S. Reyt, C. Derensart, C. Segebarth, and A. Depaulis, "Identifying neural drivers with functional MRI: An electrophysiological validation," *PLoS Biology*, vol. 6, pp. 2683–2697, 2008.
[40] K. J. Friston, L. Harrison, and W. D. Penny, "Dynamic causal modeling," *NeuroImage*, vol. 19, pp. 1273–1302, 2003.
[41] J. Ashburner *et al.*, SPM8 Manual: ch. 32, Dynamic Causal Modeling for fMRI pp. 299–312 [Online]. Available: http://www.fil.ion.ucl.ac.uk/spm/doc/manual.pdf
[42] I. W. Selesnick, "Wavelet transform with tunable Q-factor," *IEEE Trans. Sig. Proc.*, vol. 59, pp. 3560–3575, 2011.
[43] C. Louchet and L. Moisan, "Total variation as a local filter," *SIAM J. Imaging Sciences*, vol. 4, pp. 651–694, 2011.
[44] Q. J. M. Huys, M. Moutoussis, and J. Williams, "Are computational models of any use to psychiatry?," *Neural Networks*, vol. 24, pp. 544–551, 2011.
[45] *Analysis of Visual Behavior*, D. J. Ingle, M. A. Goodale, and R. J. W. Mansfield, Eds. Cambridge, MA: MIT Press, 1982.
[46] G. N. Levine, A. S. Gomes, A. E. Arai, D. A. Bluemke, S. D. Flamm, E. Kanal, W. J. Manning, E. T. Martin, J. M. Smith, N. Wilke, and F. S. Shellock, "Safety of magnetic resonance imaging in patients with cardiovascular devices," *Circulation*, vol. 116, pp. 2878–2891, 2007.
[47] H. Kato, M. Izumiyama, H. Koizumi, A. Takahashi, and Y. Itoyama, "Near-Infrared spectroscopic topography as a tool to monitor motor reorganization after hemiparetic stroke: A comparison with functional MRI," *Stroke*, vol. 33, pp. 2032–2036, 2002.
[48] K. G. Jordan, "Emergency EEG and continuous EEG monitoring in acute ischemic stroke," *J. Clin. Neurophys.*, vol. 21, pp. 341–352, 2004.
[49] P. A. Chouinard, "Changes in effective connectivity of the primary motor cortex in stroke patients after rehabilitative therapy," *Exp. Neurol.*, vol. 201, pp. 375–387, 2006.
[50] Emory University Health Sciences Center, "Parkinson's disease impacts brain's centers of touch and vision," ScienceDaily Oct. 18, 2006 [Online]. Available: http://www.sciencedaily.com/releases/2006/10/061018094705.htm
[51] J. B. Rowe, L. E. Hughes, and A. M. Owen, "Dynamic causal modeling of effective connectivity from fMRI: are results reproducible and sensitive to Parkinson's disease and its treatment?," *NeuroImage*, vol. 52, pp. 1015–1026, 2010.
[52] N. A. Kotov, J. O. Winter, I. P. Clements, E. Jan, B. P. Timko, S. Campidelli, S. Pathak, A. Mazzatenta, C. M. Lieber, M. Prato, R. V. Bellamkonda, G. A. Silva, N. Wong, S. Kam, F. Patolsky, and L. Ballerini, "Nanomaterials for neural interfaces," *Adv. Mater.*, vol. 21, pp. 1–35, 2009.
[53] J. Mehnert, C. H. Schmitz, H. E. Möller, H. Obrig, and K. Müller, "Simultaneous optical tomography (OT) and fMRI with and without task activation," in *ISMRM-ESMRMB Joint Annual Meeting*, Stockholm, Sweden, May 1–7, 2010 [Online]. Available: http://otg.downstate.edu/Publication/MehnertISMRM10.pdf

Randall L. Barbour received the Ph.D. degree in biochemistry from Syracuse University, Syracuse, NY, in 1981. This was followed by a postdoctoral fellowship in Laboratory Medicine at SUNY at Buffalo.

He is currently Professor of Pathology at SUNY Downstate Medical Center, and Research Professor of Electrical Engineering at Polytechnic University, Brooklyn, NY. He is an originator of the field of diffuse optical tomography and is co-founder of NIRx Medical Technologies, LLC. He has an extensive background in a broad range of medical and scientific and technical fields.

Harry L. Graber (M'04) received the A.B. degree in chemistry from the Washington University, St. Louis, MO, in 1983, and the Ph.D. degree in physiology and biophysics from SUNY Downstate Medical Center, Brooklyn, NY, in 1998.

He subsequently became a Research Associate (1998) and then a Research Assistant Professor (2001) at SUNY Downstate Medical Center. Also, since 2001, he has been the Senior Applications Specialist for NIRx Medical Technologies. His research interests include diffuse optical imaging algorithms, and application of feature extraction and time-series analysis methods for interpretation of biological signals.

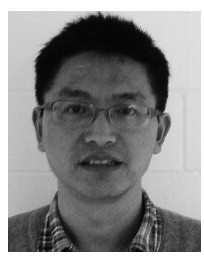

Yong Xu received the Ph.D. degree in physics from the Southwest Jiaotong University, China, in 1996. Subsequently he conducted two postdoctoral fellowships. The first was at the Institute of Applied Physics and Computational Mathematics, Beijing, China. Then he moved into the biomedical optical imaging field at Clemson University.

Since 2003, he has been a Research Assistant Professor at SUNY Downstate Medical Center, and the Assistant Director of Software Development at NIRx Medical Technologies. His research interests cover diffuse optical imaging algorithms, optical signal processing, and the applications of optical imaging in neuroscience and breast-cancer diagnosis.

Yaling Pei received the B.S. degree in structural engineering and the M.S. degree in computational mechanics from the Southwest Jiaotong University, China, in 1982 and 1986, respectively, and the Ph.D. degree in material and structural engineering from Polytechnic University, Brooklyn, NY, in 1999.

Since 2001, she has been the Director of Software Development at NIRx Medical Technologies. Her research interests cover diffuse optical imaging algorithms and optical signal processing, and the application of data-structuring, database and workflow management techniques to streamlining the analysis and interpretation of medical imaging information.

Christoph H. Schmitz received the Diploma degree in physics from the University of Bonn, Bonn, Germany, in 1995. He received the Ph.D. degree in physics from the University of Hannover, Hannover, Germany, in 1998, for work on optical-thermal laser-tissue interaction and tissue spectroscopy. He started a postdoctoral position at SUNY Downstate Medical Center, Brooklyn, NY, in 1999.

In 2001 he assumed the position of Research Assistant Professor at SUNY Downstate Medical Center. Since 2006, he has been a staff researcher at the Charité University Hospital, Berlin, Germany, and Managing Director of NIRx Medizintechnik GmbH, Berlin, Germany. His research interest is the development of diffuse optical imaging technology and its application in neuro-imaging and breast-cancer diagnosis.

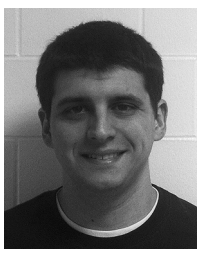

Douglas S. Pfeil received the B.S. degree in biochemistry from Lehigh University, Bethlehem, PA, in 2007. He is an M.D./Ph.D. candidate in the Molecular and Cellular Biology Program at SUNY Downstate Medical Center, Brooklyn, NY.

His research interests include near infrared imaging of the human and primate brain, particularly changes that can occur during surgery. Previously, he studied the molecular biology of nerve cell growth cones in the Wadsworth laboratory at Robert Wood Johnson University Hospital.

Anandita Tyagi received the M.S. degree in biotechnology from New York University- Polytechnic Institute, Brooklyn, in 2011.

Her research interests include near infrared imaging and spectroscopy of the human brain, and mechanisms of RNA control and transport in neurons. Previously, she studied the regulatory control of brain cytoplasmic RNA (BC RNAs) in the Physiology and Pharmacology Department of SUNY Downstate Medical Center, Brooklyn, NY.

Randy Andronica received the B.S. degree in biology from the Defiance College, Defiance. OH.

A self-taught machinist, he later supplemented his knowledge with formal training at NYC Technical College, where he returned as an adjunct lecturer on machine tool technology for a number of semesters. Prior to being employed at SUNY Downstate medical Center, he manufactured diving lights. He joined Downstate as a Biomedical Engineer, working for the Department of Scientific and Medical Instrumentation Center before joining the Optical Tomography Group, where he set up the current machine shop operation.

Daniel C. Lee received the M.D. degree from the Pritzker School of Medicine, University of Chicago. He subsequently completed a Surgery residency at Yale University and Cardiothoracic Surgery training at Cornell University and the Memorial Sloan-Kettering Cancer Center. He also completed a post-doctoral research fellowship at Columbia University.

He is currently the Medical Director of the Empire Clinical Research Investigator Program in Optical Tomography and a faculty cardiothoracic surgeon at SUNY Downstate Medical Center. His research interests are centered in the role of optical tomography in cerebral protection during cardiopulmonary bypass, breast pathology diagnosis, and neurological injury recovery.

San-Lian S. Barbour (SM'11) received the B.S. and M.S. degrees in physics. She concluded her postgraduate study in the area of electromagnetic propagation analyses using various numerical techniques and earned a professional EE degree (beyond M.S.) from Syracuse University, Syracuse, NY, in 1980.

She launched her career analyzing and developing prototypes of wideband phased array antennas at the General Electric E-Lab in Syracuse. She diversified in areas requiring multidisciplinary skills and navigated through a broad spectrum of projects including receiver RF front end PLL circuit design, analyses of antennas placed on fighter aircraft and space-based radar, linear accelerator field tuning, a patented phased array microwave hyperthermia antenna system for MRI-guided cancer treatment and wireless RF systems engineering tasks. Currently she is at Alcatel Lucent Technologies, a Bell Labs innovation company, and also leverages her acquired cross-disciplinary experiences and consults for NIRx Medical Technologies

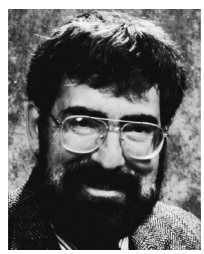

J. David Nichols received the B.S. degree in physics from Harvey Mudd College, Claremont, CA, and the M.S. and C.Phil in physics from the University California-San Diego, La Jolla.

He is a member of the technical staff at Source Signal Imaging, Inc. His current research interests involve medical image processing and creation of models for use in functional imaging.

Mark E. Pflieger was born in Columbus, OH, on August 8, 1954. He received the B.S. and Ph.D. degrees in biophysics from The Ohio State University, Columbus, in 1975 and 1991, respectively, with studies in theoretical neuroscience, cognitive psychophysiology, and neuroelectric signal processing.

Since 1990, he has been an industrial scientist in the fields of EEG/MEG and multimodal brain mapping. Currently, he is President and Senior Scientist at Source Signal Imaging, Inc., San Diego, CA, where he participates in algorithm and software development for brain research, with applications in cognitive neuroscience, neurology, and neuropsychiatry.